

# Observation of $\Gamma$ -Valley Moiré Bands and Emergent Hexagonal Lattice in Twisted Transition Metal Dichalcogenides

Ding Pei<sup>1,2,9,\*</sup>, Binbin Wang<sup>1,7,\*</sup>, Zishu Zhou<sup>3,\*</sup>, Zhihai He<sup>4,8,\*</sup>, Liheng An,<sup>3</sup> Shanmei He,<sup>2</sup> Cheng Chen,<sup>2</sup> Yiwei Li,<sup>1</sup> Liyang Wei<sup>1</sup>, Aiji Liang,<sup>1</sup> Jose Avila<sup>5</sup>, Pavel Dudin<sup>5</sup>, Viktor Kandyba,<sup>6</sup> Alessio Giampietri,<sup>6</sup> Mattia Cattelan,<sup>6</sup> Alexei Barinov,<sup>6</sup> Zhongkai Liu,<sup>1,9</sup> Jianpeng Liu,<sup>1,9</sup> Hongming Weng<sup>8,7,4</sup>, Ning Wang,<sup>3,†</sup> Jiamin Xue<sup>1,‡</sup> and Yulin Chen<sup>2,1,9,§</sup>

<sup>1</sup>*School of Physical Science and Technology, ShanghaiTech University, Shanghai 201210, China*

<sup>2</sup>*Department of Physics, University of Oxford, Oxford OX1 3PU, United Kingdom*

<sup>3</sup>*Department of Physics, the Hong Kong University of Science and Technology, Clear Water Bay, Hong Kong, China*

<sup>4</sup>*Songshan Lake Materials Laboratory, Dongguan, Guangdong 523808, China*

<sup>5</sup>*Synchrotron SOLEIL, L'Orme des Merisiers, Saint Aubin-BP 48, 91192 Gif sur Yvette Cedex, France*

<sup>6</sup>*Elettra-Sincrotrone Trieste, Trieste, Basovizza 34149, Italy*

<sup>7</sup>*School of Physical Sciences, University of Chinese Academy of Sciences, Beijing 100190, China*

<sup>8</sup>*Beijing National Laboratory for Condensed Matter Physics, and Institute of Physics, Chinese Academy of Sciences, Beijing 100190, China*

<sup>9</sup>*ShanghaiTech Laboratory for Topological Physics, ShanghaiTech University, Shanghai 200031, China*

 (Received 8 December 2021; revised 23 March 2022; accepted 23 May 2022; published 24 June 2022)

Twisted van der Waals heterostructures have recently been proposed as a condensed-matter platform for realizing controllable quantum models due to the low-energy moiré bands with specific charge distributions moiré superlattices. Here, combining angle-resolved photoemission spectroscopy with submicron spatial resolution ( $\mu$ -ARPES) and scanning tunneling microscopy (STM), we performed a systematic investigation on the electronic structure of  $5.1^\circ$  twisted bilayer  $\text{WSe}_2$  that hosts correlated insulating and zero-resistance states. Interestingly, contrary to one's expectation, moiré bands were observed only at  $\Gamma$  valley but not  $K$  valley in  $\mu$ -ARPES measurements, and correspondingly, our STM measurements clearly identified the real-space honeycomb- and kagome-shaped charge distributions at the moiré length scale associated with the  $\Gamma$ -valley moiré bands. These results not only reveal the unusual valley-dependent moiré-modified electronic structure in twisted transition metal dichalcogenides, but also highlight the  $\Gamma$ -valley moiré bands as a promising platform for exploring strongly correlated physics in emergent honeycomb and kagome lattices at different energy scales.

DOI: 10.1103/PhysRevX.12.021065

Subject Areas: Condensed Matter Physics

## I. INTRODUCTION

Moiré superlattices are formed when two layers of van der Waals (vdW) materials with a slight twist angle or lattice mismatch are stacked together. In such a superlattice, original electronic bands of the constituent layer are folded into a reduced Brillouin zone (BZ), or mini BZ, due to the enlarged moiré lattice constant, which can give rise to

isolated flat moiré bands (MBs) under suitable conditions (e.g., specific twist angle or lattice relaxation, etc.) [1–5]. At proper filling level, these moiré bands can lead to rich interesting quantum phases, such as correlated insulator [6–10], superconductor [7,8], or quantized anomalous Hall insulator [11].

In real space, a complementary view of moiré bands is the electron localization on certain positions in the moiré superlattice, forming “moiré orbitals” [5,12]. Depending on the geometry of moiré orbitals, a low-energy moiré band can be effectively described by a paradigmatic quantum model at the moiré length scale. As correlation effects and topological properties of these moiré bands can be effectively tuned by various external parameters (e.g., strain [13], substrate [14], and displacement field [9]), vdW heterostructures with moiré superlattices can be regarded as a controllable “quantum simulator” to realize different model Hamiltonians and explore their novel properties [12].

\*These authors contributed equally to this work.

†phwang@ust.hk

‡xuejm@shanghaitech.edu.cn

§yulin.chen@physics.ox.ac.uk

Published by the American Physical Society under the terms of the *Creative Commons Attribution 4.0 International license*. Further distribution of this work must maintain attribution to the author(s) and the published article's title, journal citation, and DOI.

For example, it was proposed that the flat moiré bands in the “magic-angle” twisted bilayer (TB) graphene have an equivalent real-space description as a honeycomb lattice at the moiré length scale [15–18], based on which intriguing correlated and topological states can be realized [6–8,11].

Apart from graphene-based moiré systems, twisted transition metal dichalcogenide (TMD) moiré superlattices are also gifted the versatility for studying rich emergent phases associated with different quantum systems (e.g., triangular, honeycomb, and kagome lattices) [19–22]. For examples, the  $K$ -valley moiré bands can be utilized to study the triangular Hubbard model [20,21], while the  $\Gamma$ -valley moiré bands are related to the honeycomb and kagome models [22]. Although the strongly correlated states in twisted TMDs have been revealed by recent transport results in twisted bilayer [9,10] and double-bilayer  $\text{WSe}_2$  devices [23], a direct visualization of the moiré bands in the momentum space and the associated charge distribution in the real space is still lacking.

In this work, we performed a systematic investigation on the electronic structure of  $5.1^\circ$  twisted bilayer  $\text{WSe}_2$  (TB  $\text{WSe}_2$ ), which was reported to host moiré-induced zero-resistance states [9]. By using angle-resolved photoemission spectroscopy with submicron spatial resolution ( $\mu$ -ARPES), electronic structures from both  $\Gamma$  and  $K$  valleys are directly observed. Interestingly, no sign of flat bands around  $K$  valley was seen; instead, replicalike moiré bands around  $\Gamma$  valley were clearly observed. Correspondingly, our scanning tunneling microscopy or spectroscopy (STM or STS) measurements revealed real-space charge distributions of the  $\Gamma$ -valley moiré bands at different energies, manifested as emergent honeycomb and kagome lattices at the moiré length scale. The underlying physics of these observations can be well captured by our density functional theory (DFT) and tight-binding calculations, showing that moiré potential in the twisted TMD system can significantly modify the  $\Gamma$ -valley bands, making them a unique platform for simulating different quantum systems such as honeycomb and kagome lattice models at different energy scales.

## II. RESULTS

The experimental layout and the device geometry used in this work are illustrated in Fig. 1(a). The TB  $\text{WSe}_2$  sample was fabricated using a standard tear-and-stack method [details can be found in the Appendix and in Supplemental Material (SM) [24]], which was then transferred onto the substrate composed of layers of graphite,  $h$ -BN, and  $\text{SiO}_2/\text{Si}$  [Fig. 1(a)] for flatness and electric conductivity necessary for  $\mu$ -ARPES and STM measurements. The optical image of the real device is shown in Fig. 1(b), and the  $5.1^\circ$  twist angle was confirmed by the STM measurement that shows a moiré periodicity of  $\lambda \sim 3.7$  nm [Fig. 1(c)], as  $\lambda = [a/2 \sin(\theta/2)]$  where the

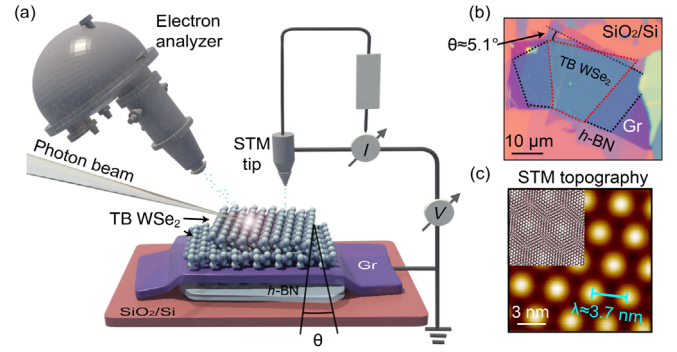


FIG. 1. Device design and experiment layout. (a) Schematic illustration of the device design and the experiment layout. From bottom to top, the red, light blue, and purple sheets stand for  $\text{SiO}_2/\text{Si}$ ,  $h$ -BN, and graphite substrates, respectively, and the atomic model stands for a bilayer  $\text{WSe}_2$  with a twist angle ( $\theta$ ). For ARPES measurements, photoelectrons are collected by a hemisphere analyzer; for STM measurements, tunneling electrons are tuned by the current ( $I$ ) and voltage ( $V$ ) sources and collected by the STM tip. (b) Optical image of  $5.1^\circ$  TB  $\text{WSe}_2$  device. Dashed lines of red and black mark boundaries of top and bottom layer  $\text{WSe}_2$ , respectively.  $\text{SiO}_2/\text{Si}$ ,  $h$ -BN, and graphite substrates appear in the same colors as shown in the illustration. The included angle of upper boundaries of top and bottom layers is the twist angle,  $\theta \approx 5.1^\circ$ . (c) STM topography, acquired at fixed bias voltage  $V_{\text{bias}} = -1.39$  V and current  $I = 90$  pA, showing the moiré pattern with a periodicity of  $\lambda \approx 3.7$  nm. The inset presents the atomic structure of TB  $\text{WSe}_2$ .

lattice constant of  $\text{WSe}_2$  was measured as  $a = 0.33$  nm (see SM for more details [24]).

A valley-resolved investigation on the electronic structure of TB  $\text{WSe}_2$  was first performed with  $\mu$ -ARPES. The consistency between the scanning photoemission microscopy (SPEM) map [Fig. 2(a)] and the optical image [Fig. 1(b)] enables us to accurately locate the measurement region on TB  $\text{WSe}_2$ . Contrary to the previous proposal that the strongly correlated states in TB  $\text{WSe}_2$  could arise from the  $K$ -valley moiré flat band, no apparent sign of moiré band around the  $K$  valley (of the top  $\text{WSe}_2$  layer, labeled as  $K_t$ ) is observed, neither in the equal energy contour mapping [Fig. 2(b)] nor in the energy-momentum dispersion across the  $K_t$  point [Fig. 2(c)]. The fact that no moiré flat bands were observed at  $K$  valley from different measurements with various photon energies and sample orientations [see Fig. 2(d) and SM [24]] rules out the suppression of the moiré bands caused by the matrix-element effect.

In contrast, additional features are observed both inside and outside the bare  $\Gamma$ -valley pocket [Fig. 2(b)] and dispersions [Figs. 2(e) and 2(f)]: replicalike moiré bands [Figs. 2(e) and 2(f), marked as MBs] can be clearly discerned in addition to the intensive main  $\Gamma$ -valley bands [Figs. 2(e) and 2(f), marked as  $\Gamma_1$  and  $\Gamma_2$ ] due to interlayer coupling of TB  $\text{WSe}_2$ . In Fig. 2(e), the momentum separation ( $\delta k$ ) between the replica and main bands is

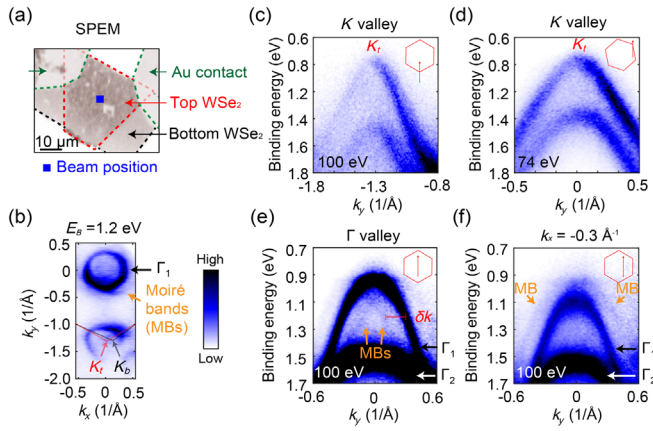


FIG. 2. ARPES measurement on TB WSe<sub>2</sub>. (a) Scanning photoemission microscopy (SPEM) of TB WSe<sub>2</sub> device. The SPEM image is generated from real-space mapping of the valence band spectra. Dashed lines of red, black, and green mark boundaries of top, bottom layer WSe<sub>2</sub>, and Au contact, respectively. The blue square marks the photon beam position during ARPES measurements. (b) Equal energy contour at binding energy  $E_B = 1.2$  eV measured at 100 eV, overlapped with BZs of the top (red) and bottom (black) layer WSe<sub>2</sub>. The subscripts  $t$  and  $b$  of  $K$  valleys stand for the top and bottom layer, respectively. The bare  $\Gamma$ -valley pocket (of main band  $\Gamma_1$ ) is indicated by the black arrow. moiré bands (MBs) are indicated by the orange arrow. (c) Band dispersion across  $K_t$  point measured at 100 eV. (d) Band dispersion across  $K_t$  point measured at 74 eV. (e) Band dispersion across  $\Gamma$  points measured at 100 eV. (f) Band dispersion along  $k_y$  at  $k_x = -0.3 \text{ \AA}^{-1}$  (around  $\Gamma$  valley) measured at 100 eV. In (c)–(f), the inset red hexagons are the BZs of top layer WSe<sub>2</sub>, showing the sample orientation, and red arrows present the directions of dispersions with respect to BZs. In (e) and (f),  $\Gamma_1$  and  $\Gamma_2$  stand for two main bands of bilayer WSe<sub>2</sub>, MBs are indicated by orange arrows,  $\delta k$  is the momentum spacing between MBs and  $\Gamma_1$ .

determined to be  $0.19 \pm 0.03 \text{ \AA}^{-1}$ , which is in consistent with the reciprocal vector of  $5.1^\circ$  TB WSe<sub>2</sub> superlattice ( $\sim 0.19 \text{ \AA}^{-1}$ ) but significantly smaller than that of the WSe<sub>2</sub>/graphite heterostructure ( $\sim 0.89 \text{ \AA}^{-1}$ ; see SM [24]) confirming the TB WSe<sub>2</sub> origin of the replica band. Other possible origins of the replica bands can also be excluded, such as the domain effect (these replica bands have been consistently observed on different positions; see SM) or umklapp scattering [25,26] of the bottom layer electronic states (as the band maximum of the monolayer WSe<sub>2</sub>  $\Gamma$  valley is significantly lower than the MB [27]).

To uncover the fine structure of the moiré bands, next we carry out STS measurements on the same sample. The  $dI/dV$  spectra from the constant-height scanning tunneling spectroscopy (CHSTS) along high-symmetry directions of the moiré lattice [AA-B-BR-B-AA; see the caption of Fig. 3(a) for definition] and three representative  $dI/dV$  curves (on AA, B, BR sites) are illustrated in Fig. 3(b), which show multiple sharp  $dI/dV$  peaks around the bias

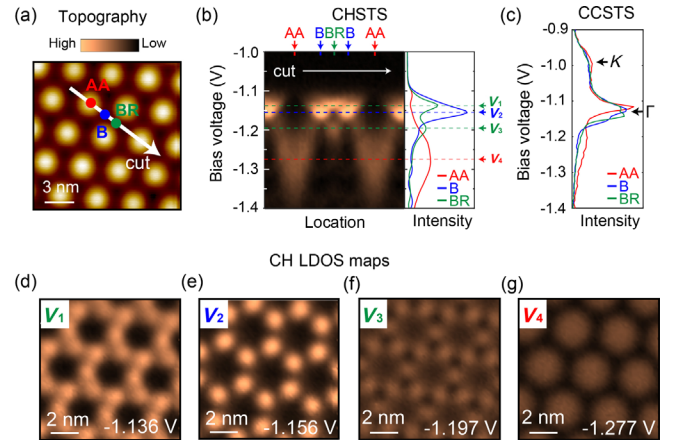


FIG. 3. STM measurement on TB WSe<sub>2</sub>. (a) Definition of high-symmetry sites in TB WSe<sub>2</sub> superlattice. Here, AA (indicated by the red point) means eclipsed stacking sites with W atoms over W atoms, BR (indicated by the green point) means the bridge that connects neighboring AA sites, and B (indicated by the blue point) stands for Bernal stacking, including two inversed configurations with W atom over Se atom ( $B_{W/Se}$ ) or Se atom over W atom ( $B_{Se/W}$ ). The white arrow indicates the direction of  $dI/dV$  spectra shown in (b). (b) Left:  $dI/dV$  spectra measured in constant height mode (CHSTS) along AA-B-BR-B-AA direction. The positions of AA, B, BR sites are indicated by arrows of corresponding colors. Right: representative  $dI/dV$  curves on AA (red), B (blue), and BR (green) sites. The peak positions in AA ( $V_4$ ), B ( $V_2$ ), and BR ( $V_1, V_3$ ) curves are marked by dashed lines of corresponding colors. (c)  $dI/dV$  curves measured in constant current mode (CCSTS) on AA, B, and BR sites. Black arrows indicate  $dI/dV$  signal contributed by  $\Gamma$  and  $K$  valleys, respectively. (d)–(g) LDOS maps (in CH mode) corresponding to the peak positions in the AA ( $V_4$ ), B ( $V_2$ ), and BR ( $V_1, V_3$ ) curves, respectively. During the LDOS mapping, the tip height was adjusted at  $V_{\text{bias}} = -1.6$  V with  $I = 170$  pA.

voltage  $V_{\text{bias}} = -1.15$  V on B and BR sites [Fig. 3(b)]. As the  $dI/dV$  signal decays exponentially with the increase of in-plane momentum of the tunneling electrons, such sharp peaks in CHSTS curves indicate the existence of flat moiré bands in the vicinity of the BZ center [28–31].

In order to extract the  $K$ -valley band information, we further carried out STS measurement in constant-current mode (CCSTS), which is more sensitive to tunneling electrons from  $K$  valleys [28]. As expected,  $dI/dV$  peaks absent in the CHSTS measurement around  $V_{\text{bias}} = -1.0$  eV are now visible as broad humps, showing the  $K$ -valley bare bands of WSe<sub>2</sub> layers (see SM for identification methods [24]) but no sign of sharp peaks as those observed from the  $\Gamma$  valley at  $V_{\text{bias}} = -1.15$  V (visible in both CHSTS and CCSTS curves).

Interestingly, if we map out the local density of state (LDOS) distribution in real space at different  $dI/dV$  peak energies [ $V_1$ – $V_4$ , as marked in Fig. 3(b)], one can see different moiré orbital symmetry. As shown in Figs. 3(d)–3(g), the LDOS maps from STM measurements

where bias voltages were set to  $dI/dV$  peaks from AA [ $V_4$ , Fig. 3(g)] and B [ $V_2$ , Fig. 3(e)] sites both show honeycomb lattice, while the LDOS maps with  $V_{\text{bias}}$  set to the  $dI/dV$  peaks from BR site [ $V_1$  for Fig. 3(d) and  $V_3$  for Fig. 3(f)] clearly show kagome-type patterns. The observed charge distribution complies with a  $D_6$  symmetry at the moiré length scale instead of the  $D_3$  symmetry of the TB WSe<sub>2</sub> moiré superlattice as a result of the emergent  $D_6$  symmetry of moiré potential, since the  $z$  to  $-z$  (the out-of-plane direction) reflection in lattice structure does not affect the overall moiré potential of a bilayer system [22]. [This is supported by the qualitatively identical  $dI/dV$  spectra on the neighboring B sites with inversed configurations [Fig. 3(b).] According to the continuum theory [22], the emergence of kagome lattice in twisted TMDs is related with the  $sd_2$  hybridization of moiré orbitals on Bernal stacking regions, which moves the Wannier centers from neighboring B sites to the middle point, i.e., BR sites, thus turning a honeycomb lattice to a kagome lattice.

To understand the above experimental observations, we performed both first-principles and tight-binding calculations. Notations of high-symmetry points in the mini BZ of

TB WSe<sub>2</sub> superlattice are illustrated in Fig. 4(a). In the first-principles calculation [Fig. 4(b), left-hand part], we find a set of less dispersive bands (highlighted in red) located around 0.25 eV below the valence band maximum (VBM). The calculated charge distributions corresponding to these bands appear as honeycomb or kagome patterns at different binding energies [Fig. 4(d), right-hand part;  $e_1$  for the honeycomb pattern,  $e_2$  for the kagome pattern], which qualitatively agrees with our observations. To validate the origin of these flat bands, the unfolding procedure based on the atomistic tight-binding model has been utilized [32,33]. Unfolding the moiré band structures can be simply understood as the projection of calculated moiré wave functions onto wave functions of each monolayer WSe<sub>2</sub>, which presents the weighted (based on the projection) moiré bands in the original BZ [as illustrated in Fig. 4(c)]. In the tight-binding calculation [Fig. 4(d), left-hand part], qualitatively equivalent moiré bands (highlighted in red) with similar range of binding energy are observed, confirming the consistency between the first-principles and tight-binding calculations. In the unfolded band structure along the  $K$ - $\Gamma$ - $M$  direction [Fig. 4(c), right-hand part], we can immediately find these flat bands are the topmost  $\Gamma$ -valley moiré bands (the equivalent energies to  $e_1$  and  $e_2$  are indicated by the red dashed lines). Thus, we conclude the honeycomb and kagome models are intrinsic properties of  $\Gamma$ -valley moiré bands.

### III. DISCUSSION AND CONCLUSION

While the absence of  $K$ -valley flat bands in both  $\mu$ -ARPES and STM or STS measurements (the  $\Gamma$ -valley moiré bands are clearly observed) may seem unexpected, it could be understood from the  $K$ -valley orbital components [34]: in each constituent WSe<sub>2</sub> layer, the  $K$ -valley bands are contributed by orbitals with in-plane orientation (metals'  $d_{xy}$ ,  $d_{x^2-y^2}$  and chalcogens'  $p_x$ ,  $p_y$  orbitals), which are weakly coupled between layers due to the small interlayer overlap of their wave functions; while for  $\Gamma$  valley, the bands are formed by metals'  $d_{z^2}$  and chalcogens'  $p_z$  orbitals, which naturally have larger overlap (thus interlayer coupling). Indeed, the continuum theory predicts the moiré potential in the  $K$ -valley model is less than one-fifth of that in the  $\Gamma$ -valley model [20–22]. Displacement field, which is indispensable in realizing strongly correlated phases in twisted TMDs, could be the key factor for the enhancement of moiré potential effects on the  $K$ -valley bands. Further ARPES and STM experiments with electrostatic gating are needed to search for the  $K$ -valley moiré bands in 5.1° TB WSe<sub>2</sub>.

The  $\Gamma$ -valley moiré bands have narrow band widths [see Figs. 3(b) and 3(c)] favorable for hosting strongly correlated phases. Moreover, the fact that the real-space LDOS mapping at the  $dI/dV$  peak energy shows different (honeycomb- and kagome-shaped) charge distribution at the moiré length scale indicates the  $\Gamma$ -valley moiré bands can serve as a flexible platform to realize controllable

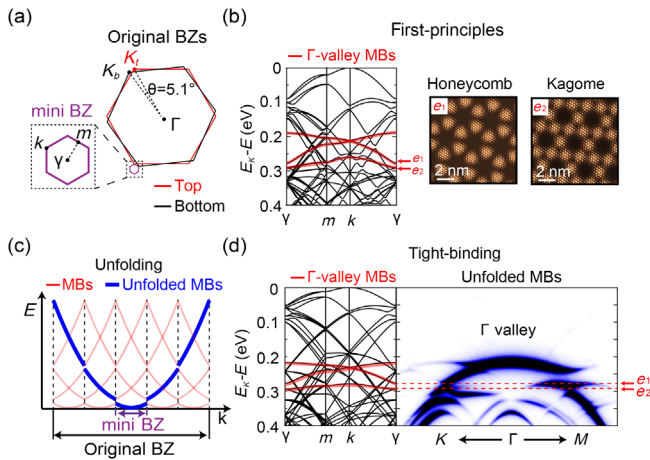


FIG. 4. Calculation on TB WSe<sub>2</sub>. (a) Original BZs of a bilayer WSe<sub>2</sub> with a twist angle  $\theta = 5.1^\circ$  and resulting mini BZ of TB WSe<sub>2</sub> superlattices. The BZs of top layer, bottom layer WSe<sub>2</sub>, and the mini BZ of TB WSe<sub>2</sub> are illustrated in red, black, and purple, respectively. High-symmetry points are labeled on BZs; the subscripts  $t$  and  $b$  stand for the top and bottom layer, respectively. (b) Left: first-principles-calculated moiré bands (MBs) of 5.1° TB WSe<sub>2</sub> presented in the mini BZ. The top three  $\Gamma$ -valley MBs are highlighted in red. Right: calculated charge distributions at energies  $e_1$  and  $e_2$  (indicated by red arrows in the left-hand part), showing honeycomb ( $e_1$ ) and kagome patterns ( $e_2$ ). (c) A simplified example illustrating the band unfolding in 1D (more discussion of 2D case can be found in SM [24]). Blue and red lines show the unfolded and folded bands. (d) Left: tight-binding-calculated MBs of 5.1° TB WSe<sub>2</sub> presented in the mini BZ. The top three  $\Gamma$ -valley MBs are highlighted in red. Right: the unfolded MBs around  $\Gamma$  valley (along  $K$ - $\Gamma$ - $M$  direction in the original BZ). The equivalent positions of  $e_1$  and  $e_2$  are indicated by red arrows and dashed lines.

honeycomb and kagome quantum model systems, which may host rich correlated and topological states at proper fillings [35,36]. This scenario is experimentally feasible, as the majority of 2H-phase TMD homomultilayers (e.g.,  $\text{WS}_2$ ,  $\text{MoS}_2$ , and  $\text{MoSe}_2$ ) [27,37,38] and heteromultilayers (e.g.,  $\text{MoS}_2/\text{WS}_2$  bilayer) [39] have their VBM at the  $\Gamma$  point, and thus the  $\Gamma$ -valley moiré bands would dominate their electric properties via electrostatic gating. (The  $\Gamma$ -valley moiré bands of TB  $\text{WSe}_2$  can also be pushed up to the VBM when in-plane lattice constant increases by  $\sim 2.5\%$ ; see SM [24].) Indeed, recent transport measurements on twisted double-bilayer  $\text{WSe}_2$  whose VBM is at the  $\Gamma$  point [23] have already revealed strongly correlated phases result from the  $\Gamma$ -valley moiré bands.

In conclusion, our results point out the importance of the  $\Gamma$ -valley moiré bands in the twisted TMDs, which gives a new direction for the exploration of correlated states in honeycomb and kagome models.

## ACKNOWLEDGMENTS

B. W. and J. X. acknowledge financial support from the Ministry of Science and Technology of China (2017YFA0305400) and the Strategic Priority Research Program of Chinese Academy of Sciences (XDA18010000), and experimental support from the Soft Nano Fabrication Center at ShanghaiTech. D. P. and S. H. thank the China Scholarship Council for support. Y. L. acknowledges the support from the National Natural Science Foundation of China (No. 12104304) and China Postdoctoral Science Foundation (No. 2021M692131). H. W. acknowledges the support from the National Natural Science Foundation of China (No. 2018YFA-0305700, No. XDB33000000, No. 11925408, and No. 12188101). Z. Z., L. A., and N. W. thank the National Key R&D Program of China (2020YFA0309600) and the Hong Kong Research Grants Council (Project No. 16303720) for support. D. P. is thankful for the useful discussion with Niels B. M. Schröter. The micro-ARPES research in SOLEIL is under Proposal No. 20210047. The research leading to micro-ARPES results in Elettra under Proposal No. 20195301 has been supported by the project CALIPSO+ under Grant Agreement No. 730872 from the EU Framework Program for Research and Innovation HORIZON 2020. Preliminary ARPES experiments were performed at nano-ARPES branch of BL07U end station, SSRF. The computational resource is provided by the Platform for Data-Driven Computational Materials Discovery in Songshan Lake material Laboratory.

## APPENDIX: METHODS

### 1. Sample preparation

The TB  $\text{WSe}_2$  device was fabricated by using dry-transfer technique. The monolayer and few-layers  $\text{WSe}_2$  flakes were mechanically exfoliated from bulk crystal onto

the  $\text{SiO}_2$  wafer. Polycarbonate film was used to tear part of the target monolayer  $\text{WSe}_2$  at around  $80^\circ\text{C}$ – $100^\circ\text{C}$ . The left-hand part of  $\text{WSe}_2$  was rotated manually by a twist angle ( $\theta$ ) around  $5.1^\circ$  ( $\pm 0.1^\circ$ ) and stacked together. For the substrate part, few-layers boron nitride films with a thickness of 10 to 20 nm were exfoliated on the silicon wafer. Then 4–5-layers graphite thin films were picked up by polycarbonate film and transferred onto the prepared boron nitride. Then the TB  $\text{WSe}_2$  was transferred onto the graphite thin film. Finally, an electrode of Cr (5 nm) and Au (7 nm) was deposited on part of the graphite films to form the contact.

### 2. $\mu$ -ARPES measurement

Samples were annealed at  $300^\circ\text{C}$  for 4 h before ARPES measurements. All experiments were performed with a base vacuum better than  $3 \times 10^{-10}$  mbar. Experiments at the SpectroMicroscopy beam line of Elettra Sincrotrone Trieste were performed at 94 K with photon energies of 27 and 74 eV, polarization of linear horizontal (LH). The estimated energy and angular resolutions were  $\sim 50$  meV and  $0.3^\circ$ , respectively. Experiments at the analysis nano-spot angle-resolved photoemission spectroscopy (ANTARES) beam line of Synchrotron SOLEIL were performed at 75 K with a photon energy of 100 eV, polarization of LH. The estimated energy and angular resolutions were  $\sim 40$  meV and  $0.5^\circ$ , respectively.

### 3. STM measurement

The STM and STS measurements were performed under ultrahigh vacuum (pressure  $\leq 10^{-11}$  mbar) and liquid helium temperature with an Omicron low-temperature STM. The etched tungsten wires were used as the STM tip. The constant-height  $dI/dV$  spectroscopy was acquired by turning off the feedback loop and using the standard lock-in techniques ( $f = 991.7$  Hz,  $V_{\text{amp}} = 4$  mV). The constant-current  $dI/dV$  spectroscopy was acquired by leaving on the feedback loop. The tip-sample distance  $Z$  changed to keep the constant tunneling current. The tip was calibrated on Ag (111) before measurements on the samples. STM or STS data were analyzed using SPIP 6.7.3 and MATLAB.

### 4. Calculation

The first-principle calculations are performed by using the Vienna *ab initio* simulation package [40] with the projector-augmented wave potential method [41–43]. The exchange-correlation potential is described using the generalized gradient approximation in the Perdew-Burke-Ernzerhof form [44]. The energy cutoff of the plane-wave basis set is 300 eV. A vacuum region larger than  $15 \text{ \AA}$  is applied to ensure no interaction between the slab and its image. In our optimization, all structures are relaxed until the force on each atom is less than  $0.01 \text{ eV/\AA}$ .

The van der Waals interactions between the adjacent layers are considered by using zero damping DFT-D3 method of Grimme [45].

We unfold the bands of twisted bilayer to the primitive-cell BZ of a monolayer [32,33]. The tight-binding method is adopted to calculate the unfolded bands of twisted bilayer WSe<sub>2</sub>. The band structure of monolayer WSe<sub>2</sub> can be described by a tight-binding Hamiltonian consisting of 11 atomic orbitals, the *d* orbitals for W, and the *p* orbitals for Se. Here, we consider the first-neighbor W-W, Se-Se, W-Se hopping terms and the second-neighbor W-Se hopping term to improve the accuracy. The tight-binding parameters are obtained by fitting the low-energy conduction and valence bands, which are given in Table S1 of Supplemental Material [24]. The effect of spin-orbit coupling (SOC) is included by adding an on-site term  $\sum_{\alpha} \lambda_{\alpha} \mathbf{L} \cdot \mathbf{S}$  in the Hamiltonian, where  $\alpha$  stands W or Se atom. The parameters of SOC terms are taken from Ref. [46]. More details are available in SM [24].

- 
- [1] E. Y. Andrei and A. H. MacDonald, *Graphene Bilayers with a Twist*, *Nat. Mater.* **19**, 1265 (2020).
- [2] L. Balents, C. R. Dean, D. K. Efetov, and A. F. Young, *Superconductivity and Strong Correlations in moiré Flat Bands*, *Nat. Phys.* **16**, 725 (2020).
- [3] S. Carr, S. Fang, and E. Kaxiras, *Electronic-Structure Methods for Twisted moiré Layers*, *Nat. Rev. Mater.* **5**, 748 (2020).
- [4] E. Y. Andrei, D. K. Efetov, P. Jarillo-Herrero, A. H. MacDonald, K. F. Mak, T. Senthil, E. Tutuc, A. Yazdani, and A. F. Young, *The Marvels of moiré Materials*, *Nat. Rev. Mater.* **6**, 201 (2021).
- [5] J. Liu and X. Dai, *Orbital Magnetic States in moiré Graphene Systems*, *Nat. Rev. Phys.* **3**, 367 (2021).
- [6] Y. Cao, V. Fatemi, A. Demir, S. Fang, S. L. Tomarken, J. Y. Luo, J. D. Sanchez-Yamagishi, K. Watanabe, T. Taniguchi, E. Kaxiras *et al.*, *Correlated Insulator Behaviour at Half-Filling in Magic-Angle Graphene Superlattices*, *Nature (London)* **556**, 80 (2018).
- [7] Y. Cao, V. Fatemi, S. Fang, K. Watanabe, T. Taniguchi, E. Kaxiras, and P. Jarillo-Herrero, *Unconventional Superconductivity in Magic-Angle Graphene Superlattices*, *Nature (London)* **556**, 43 (2018).
- [8] X. Lu, P. Stepanov, W. Yang, M. Xie, M. A. Aamir, I. Das, C. Urgell, K. Watanabe, T. Taniguchi, G. Zhang *et al.*, *Superconductors, Orbital Magnets and Correlated States in Magic-Angle Bilayer Graphene*, *Nature (London)* **574**, 653 (2019).
- [9] L. Wang, E. M. Shih, A. Ghiotto, L. Xian, D. A. Rhodes, C. Tan, M. Claassen, D. M. Kennes, Y. Bai, B. Kim *et al.*, *Correlated Electronic Phases in Twisted Bilayer Transition Metal Dichalcogenides*, *Nat. Mater.* **19**, 861 (2020).
- [10] A. Ghiotto, E.-M. Shih, G. S. S. G. Pereira, D. A. Rhodes, B. Kim, J. Zang, A. J. Millis, K. Watanabe, T. Taniguchi, J. C. Hone *et al.*, *Quantum Criticality in Twisted Transition Metal Dichalcogenides*, *Nature (London)* **597**, 345 (2021).
- [11] M. Serlin, C. L. Tschirhart, H. Polshyn, Y. Zhang, J. Zhu, K. Watanabe, T. Taniguchi, L. Balents, and A. F. Young, *Intrinsic Quantized Anomalous Hall Effect in a moiré Heterostructure*, *Science* **367**, 900 (2020).
- [12] D. M. Kennes, M. Claassen, L. Xian, A. Georges, A. J. Millis, J. Hone, C. R. Dean, D. N. Basov, A. N. Pasupathy, and A. Rubio, *moiré Heterostructures as a Condensed-Matter Quantum Simulator*, *Nat. Phys.* **17**, 155 (2021).
- [13] N. P. Kazmierczak, M. Van Winkle, C. Ophus, K. C. Bustillo, S. Carr, H. G. Brown, J. Ciston, T. Taniguchi, K. Watanabe, and D. K. Bediako, *Strain Fields in Twisted Bilayer Graphene*, *Nat. Mater.* **20**, 956 (2021).
- [14] H. S. Arora, R. Polski, Y. Zhang, A. Thomson, Y. Choi, H. Kim, Z. Lin, I. Z. Wilson, X. Xu, J.-H. Chu *et al.*, *Superconductivity in Metallic Twisted Bilayer Graphene Stabilized by WSe<sub>2</sub>*, *Nature (London)* **583**, 379 (2020).
- [15] E. Suárez Morell, J. D. Correa, P. Vargas, M. Pacheco, and Z. Barticevic, *Flat Bands in Slightly Twisted Bilayer Graphene: Tight-Binding Calculations*, *Phys. Rev. B* **82**, 121407 (2010).
- [16] R. Bistritzer and A. H. MacDonald, *Moiré Bands in Twisted Double-Layer Graphene*, *Proc. Natl. Acad. Sci. U.S.A.* **108**, 12233 (2011).
- [17] J. Kang and O. Vafek, *Symmetry, Maximally Localized Wannier States, and a Low-Energy Model for Twisted Bilayer Graphene Narrow Bands*, *Phys. Rev. X* **8**, 031088 (2018).
- [18] H. C. Po, L. Zou, A. Vishwanath, and T. Senthil, *Origin of Mott Insulating Behavior and Superconductivity in Twisted Bilayer Graphene*, *Phys. Rev. X* **8**, 031089 (2018).
- [19] M. H. Naik and M. Jain, *Ultraflatbands and Shear Solitons in Moiré Patterns of Twisted Bilayer Transition Metal Dichalcogenides*, *Phys. Rev. Lett.* **121**, 266401 (2018).
- [20] F. Wu, T. Lovorn, E. Tutuc, and A. H. MacDonald, *Hubbard Model Physics in Transition Metal Dichalcogenide Moiré Bands*, *Phys. Rev. Lett.* **121**, 026402 (2018).
- [21] F. Wu, T. Lovorn, E. Tutuc, I. Martin, and A. H. MacDonald, *Topological Insulators in Twisted Transition Metal Dichalcogenide Homobilayers*, *Phys. Rev. Lett.* **122**, 086402 (2019).
- [22] M. Angeli and A. H. MacDonald, *Valley Transition Metal Dichalcogenide Moiré Bands*, *Proc. Natl. Acad. Sci. U.S.A.* **118**, e2021826118 (2021).
- [23] L. An, X. Cai, D. Pei, M. Huang, Z. Wu, Z. Zhou, J. Lin, Z. Ying, Z. Ye, X. Feng *et al.*, *Interaction Effects and Superconductivity Signatures in Twisted Double-Bilayer WSe<sub>2</sub>*, *Nanoscale Horiz.* **5**, 1309 (2020).
- [24] See Supplemental Material at <http://link.aps.org/supplemental/10.1103/PhysRevX.12.021065> for additional ARPES and STM data, technical details for calculation, and data analysis.
- [25] S. Ulstrup, R. J. Koch, S. Singh, K. M. McCreary, B. T. Jonker, J. T. Robinson, C. Jozwiak, E. Rotenberg, A. Bostwick, J. Katoch *et al.*, *Direct Observation of Minibands in a Twisted Graphene/WSe<sub>2</sub> Bilayer*, *Sci. Adv.* **6**, eaay6104 (2020).
- [26] S. Xie, B. D. Faeth, Y. Tang, L. Li, C. T. Parzyck, D. Chowdhury, Y.-H. Zhang, C. Jozwiak, A. Bostwick, E. Rotenberg *et al.*, *Strong Interlayer Interactions in Bilayer*

- and Trilayer Moiré Superlattices, *Sci. Adv.* **8**, eabk1911 (2022).
- [27] Y. Zhang, M. M. Ugeda, C. Jin, S.-F. Shi, A. J. Bradley, A. Martín-Recio, H. Ryu, J. Kim, S. Tang, Y. Kim *et al.*, *Electronic Structure, Surface Doping, and Optical Response in Epitaxial WSe<sub>2</sub> Thin Films*, *Nano Lett.* **16**, 2485 (2016).
- [28] C. Zhang, Y. Chen, A. Johnson, M.-Y. Li, L.-J. Li, P. C. Mende, R. M. Feenstra, and C.-K. Shih, *Probing Critical Point Energies of Transition Metal Dichalcogenides: Surprising Indirect Gap of Single Layer WSe<sub>2</sub>*, *Nano Lett.* **15**, 6494 (2015).
- [29] Z. Zhang, Y. Wang, K. Watanabe, T. Taniguchi, K. Ueno, E. Tutuc, and B. J. LeRoy, *Flat Bands in Twisted Bilayer Transition Metal Dichalcogenides*, *Nat. Phys.* **16**, 1093 (2020).
- [30] H. Li, S. Li, M. H. Naik, J. Xie, X. Li, J. Wang, E. Regan, D. Wang, W. Zhao, S. Zhao *et al.*, *Imaging Moiré Flat Bands in Three-Dimensional Reconstructed WSe<sub>2</sub>/WS<sub>2</sub> Superlattices*, *Nat. Mater.* **20**, 945 (2021).
- [31] E. Li, J.-X. Hu, X. Feng, Z. Zhou, L. An, K. T. Law, N. Wang, and N. Lin, *Lattice Reconstruction Induced Multiple Ultra-Flat Bands in Twisted Bilayer WSe<sub>2</sub>*, *Nat. Commun.* **12**, 5601 (2021).
- [32] H. Nishi, Y.-i. Matsushita, and A. Oshiyama, *Band-Unfolding Approach to Moiré-Induced Band-Gap Opening and Fermi Level Velocity Reduction in Twisted Bilayer Graphene*, *Phys. Rev. B* **95**, 085420 (2017).
- [33] Y.-i. Matsushita, H. Nishi, J.-i. Iwata, T. Kosugi, and A. Oshiyama, *Unfolding Energy Spectra of Double-Periodicity Two-Dimensional Systems: Twisted Bilayer Graphene and Mos<sub>2</sub> on Graphene*, *Phys. Rev. Mater.* **2**, 010801 (2018).
- [34] J. Á. Silva-Guillén, P. San-Jose, and R. Roldán, *Electronic Band Structure of Transition Metal Dichalcogenides from Ab Initio and Slater-Koster Tight-Binding Model*, *Appl. Sci.* **6**, 284 (2016).
- [35] T. Neupert, L. Santos, C. Chamon, and C. Mudry, *Fractional Quantum Hall States at Zero Magnetic Field*, *Phys. Rev. Lett.* **106**, 236804 (2011).
- [36] E. Tang, J.-W. Mei, and X.-G. Wen, *High-Temperature Fractional Quantum Hall States*, *Phys. Rev. Lett.* **106**, 236802 (2011).
- [37] W. Jin, P.-C. Yeh, N. Zaki, D. Zhang, J. T. Sadowski, A. Al-Mahboob, A. M. van der Zande, D. A. Chenet, J. I. Dadap, I. P. Herman *et al.*, *Direct Measurement of the Thickness-Dependent Electronic Band Structure of Mos<sub>2</sub> Using Angle-Resolved Photoemission Spectroscopy*, *Phys. Rev. Lett.* **111**, 106801 (2013).
- [38] Y. Zhang, T.-R. Chang, B. Zhou, Y.-T. Cui, H. Yan, Z. Liu, F. Schmitt, J. Lee, R. Moore, Y. Chen *et al.*, *Direct Observation of the Transition from Indirect to Direct Bandgap in Atomically Thin Epitaxial MoSe<sub>2</sub>*, *Nat. Nanotechnol.* **9**, 111 (2014).
- [39] A. J. H. Jones, R. Muzzio, S. Pakdel, D. Biswas, D. Curcio, N. Lanatà, P. Hofmann, K. M. McCreary, B. T. Jonker, K. Watanabe *et al.*, *Visualizing Band Structure Hybridization and Superlattice Effects in Twisted MoS<sub>2</sub>/WS<sub>2</sub> Heterobilayers*, *2D Mater.* **9**, 015032 (2022).
- [40] G. Kresse and J. Hafner, *Ab Initio Molecular Dynamics for Liquid Metals*, *Phys. Rev. B* **47**, 558 (1993).
- [41] P. E. Blöchl, *Projector Augmented-Wave Method*, *Phys. Rev. B* **50**, 17953 (1994).
- [42] G. Kresse and J. Furthmüller, *Efficient Iterative Schemes for Ab Initio Total-Energy Calculations Using a Plane-Wave Basis Set*, *Phys. Rev. B* **54**, 11169 (1996).
- [43] G. Kresse and D. Joubert, *From Ultrasoft Pseudopotentials to the Projector Augmented-Wave Method*, *Phys. Rev. B* **59**, 1758 (1999).
- [44] J. P. Perdew, K. Burke, and M. Ernzerhof, *Generalized Gradient Approximation Made Simple*, *Phys. Rev. Lett.* **77**, 3865 (1996).
- [45] S. Grimme, J. Antony, S. Ehrlich, and H. Krieg, *A Consistent and Accurate Ab Initio Parametrization of Density Functional Dispersion Correction (DFT-D) for the 94 Elements H-Pu*, *J. Chem. Phys.* **132**, 154104 (2010).
- [46] S. Fang, R. Kuate Defo, S. N. Shirodkar, S. Lieu, G. A. Tritsarlis, and E. Kaxiras, *Ab Initio Tight-Binding Hamiltonian for Transition Metal Dichalcogenides*, *Phys. Rev. B* **92**, 205108 (2015).